International Journal of Multiphase Flow 36 (2010) 234–243

Contents lists available at ScienceDirect

International Journal of Multiphase Flow

journal homepage: www.elsevier.com/locate/ijmulflow

Particle statistics in a gas–solid coaxial strongly swirling flow: A direct numerical simulation

Nan Gui, JianRen Fan *, Zhe Zhou

State Key Laboratory of Clean Energy Utilization, Zhejiang University, Hangzhou 310027, PR China

ARTICLE INFO

Article history:
Received 10 February 2009
Received in revised form 22 September 2009
Accepted 5 October 2009
Available online 29 October 2009

Keywords:
Direct numerical simulation
Particle dispersion
Coaxial swirling flow
Particle-laden flow
Particle statistics
Eulerian–Lagrangian approach

ABSTRACT

A direct numerical simulation of a strongly coaxial swirling particle-laden flow is conducted with reference to a previous experiment. The carrier phase is simulated as a coaxial swirling flow through a short nozzle injecting into a large container. The particle phase is carried by the primary jet, and simulated in the Lagrangian approach. The drag force, slip-shear force and slip-rotation force experienced by particles are calculated. A partial validation of the results is followed. The results are analyzed in Eulerian approach focusing on the statistical behavior of particle motion. The relative importance of the drag, slip-shear and slip-rotation forces under different Stokes numbers is indicated quantitatively. The particle velocity profiles, fluctuations, Reynolds stress, and turbulence intensity are demonstrated and analyzed respectively. An important "choke" behavior for large particles within the mainstream is found and interpreted. Additionally, the patterns of particle distribution and the helical structures of particle motion under different Stokes numbers are demonstrated qualitatively and analyzed quantitatively.

1. Introduction

Particle-laden coaxial swirling jets are widely used in a variety of engineering applications. For example, cyclone separators are commonly used to separate particles from a particle-laden flow by the strong centrifugal force exerted on the particles. Due to the occurrence of a central recirculation zone in strongly swirling flows, swirl can be used to stabilize non-premixed flames and establish high mixing rates, in which a drastic mixing between the fuel and the swirling air stream is obtained (Sommerfeld and Qiu, 1993).

Extensive research efforts have been expended on improving the understanding of the aerodynamics of the swirling flow and characterizing the physical structures of swirling flows. For example, with regards to the intriguing phenomenon of vortex breakdown in swirling flows, Benjamin (1962) characterized the vortex breakdown as a finite transition between two dynamically conjugate states of axisymmetric flow, analogous to a hydraulic jump in an open channel flow. Escudier and Zehnder (1982) suggested a criterion for the occurrence of vortex breakdown in a tube, by a relationship between the pipe Reynolds number and the product of the circulation number and the ratio of the radial to tangential velocities. Billant et al. (1998) and Liang and Maxworthy (2005) carried out experimental investigations of swirling jets, focusing on the different types of vortex breakdown phenomena and the various dynamical mechanisms related to it. Herrada and Shtern (2003) showed the vortex breakdown control by a combination of additional near-axis swirl and heat. They addressed a flow in a cylindrical container driven by a rotating bottom disk, and carried out a numerical analysis on explanation of the experimentally observed effect of control of co-rotation and counter-rotation.

Moreover, on other aspects of the swirl flow, Grauer and Sideris (1991) implemented a numerical computation of three-dimensional incompressible ideal fluids with swirl, in which the Euler equation is reduced to a two-dimensional problem using rotational symmetry. Shtern et al. (1994) and Shtern and Mi (2004) studied generation, hysteresis and precession of a swirling jet. They demonstrated the feasibility of a supercritical pitchfork bifurcation from an initially trivial non-swirling flow to one with a steady swirling regime, and showed that hysteresis is a common feature of wall-normal vortices or swirling jets no matter where the sources of motion are located. They also studied the jet stability, especially a half-line vortex normal to a rigid plane, with the aid of a new approach accounting for deceleration and non-parallelism of the base flow, and reduced the stability problem to a set of ordinary differential equations.

However, to study the aerodynamics of fluid phase, isothermal swirling flows only provides a foundation stone and acts as the first step to understanding the complex reacting swirling flows. Since the swirling flow is most widely used in combustion systems in which the flow structure under combusting conditions deviate considerably from that of isothermal swirling flows. Moreover, the motion of the dispersed phase is also of great significance to

* Corresponding author. Fax: +86 0571 87991863.
E-mail address: fanjr@zju.edu.cn (J. Fan).

0301-9322/$ - see front matter © 2009 Elsevier Ltd. All rights reserved.
doi:10.1016/j.ijmultiphaseflow.2009.10.003

be studied. Thus, to study the particle-laden incompressible swirling flow is the secondary step to improve the knowledge of the swirling multiphase flow. The general objectives are to study the coupling effects of the carrier phase and the dispersed phase, especially the effects of different operating conditions and influencing factors on the motion of the dispersed phase.

For example, Park et al. (1998) presented direct numerical simulation of a droplet-laden swirling jet, examined the effects of swirl and two-phase momentum coupling on the jet dynamics and structural characteristics. They indicated that the dynamics of large-scale structures are strongly affected by the degree of swirl imparted to the jet, and the jet dynamics and time-averaged behavior are strongly affected by both the inter-phase momentum coupling and swirl intensity. The momentum coupling reduces the shear layer growth, mixing and entrainment rate for weakly and moderately swirling jets, and it becomes even dramatic for strongly swirling jets, etc. Wicker and Eaton (2001) carried out an experimental study on the structure of a swirling coaxial free jet and its effect on particle motion, with Reynolds number Re = 13,000, swirl number $S = 0.92$, and five particle Stokes numbers ranging from 1 to 5. They focused on the toroidal structure and its effect on particle dispersion, and found the coherent structures disperse particles more effectively than the natural jet. Shirolkar and Mcquay (2001) applied a PDF propagation approach to model turbulent dispersion in swirling flows. They used two different turbulence models to solve the fluid phase, and the models are evaluated with experiments of Sommerfeld and Qiu (1993). Their results demonstrated the computational efficiency of the model, and compared favorably with the experimental data. Apte et al. (2003) and Oefelein et al. (2007) both carried out large eddy simulations of coaxial swirling particle-laden flows in a combustor. Their simulations tracked particle motion under the Lagrangian frame and treated particle as a point source term for inter-phase momentum exchange. More interestingly, on the micro-length scale when the fluid inertia is important, Subramanian and Koch (2006) studied suspensions of neutrally buoyant particles subject to simple shear flow, and showed that micro-scale inertia dramatically alters the streamline topology and the heat or mass transfer when Re is kept small. Moreover, in an analytical way, Candelier and Angilella (2006) treated with the explicit contribution of each term appearing in the perturbed flow equation by using matched asymptotic expansions. They analyzed the explicit contribution of fluid inertia and fluid unsteadiness to the force acting on a solid sphere moving in a vertical solid-body rotation flow, under the limit of small Reynolds and Taylor numbers, and showed how the convective terms and the unsteady term contribute to the particle drag and lift coefficients in a very complex and non-additive manner.

In conclusion, particle-laden swirling flow is of great significance in both industrial application and scientific research. More specifically, particle motion under different operating conditions is required to be studied to show the relative importance of the centrifugal and advective motions. However, very few researches have been done on the characteristics of particle behavior influenced by the anisotropic nature of swirling vortex. Moreover, DNS is a promising numerical approach for improving the understanding of both the swirling flow structure and the particle dispersion behaviors. It can provide full scales of turbulence by a set of very fine grids and high order difference schemes, though it is usually implemented at low Reynolds numbers due to the computer performance limitation. Thus, the present study used DNS to study the particle dispersion in a strongly swirling flow, focusing on the statistical behavior of particle motion and the influencing factors for them. The flow conditions and parameters used in this numerical simulation are mainly according to a previous experimental study of a particle-laden confined swirling flow carried out by Sommerfeld and Qiu (1993), but with somewhat changes due to simulation limitation and for facilitation of the numerical treatment.

2. Numerical description

2.1. Governing equations of fluid

In the preset study, the full three-dimensional, time-dependent, incompressible Navier–Stokes equations of viscous Newtonian fluids are solved directly on structured grids with its resolution meets the requirement of direct numerical simulation. The continuity of mass and conservation of momentum are formulated in the non-dimensional form as following:

$$\nabla \cdot \mathbf{u} = 0 \tag{1}$$

$$\frac{\partial \mathbf{u}}{\partial t} + (\mathbf{u} \cdot \nabla)\mathbf{u} = -\nabla p + \frac{1}{\mathrm{Re}}\nabla^2 \mathbf{u} + \mathbf{F}_b \tag{2}$$

where $\mathbf{u}$ is fluid velocity and p is pressure. The Reynolds number $\mathrm{Re} = \frac{D_2 U_1}{\nu}$ is defined based on the diameter of the annular swirling flow D_2 and the mean velocity of the primary flow U_1. $\mathbf{F}_b$ is the particle-to-fluid feedback force in discretized control volumes, and it is a sum of all feedback forces of particles in the control volume: $\mathbf{F}_b = \sum_{i=1}^{N} \boldsymbol{f}_{b,i}$, where N is the instantaneous number of particles in the control volume and $f_{b,i}$ is the feedback force from the 'i' th particle to fluid.

To solve the above equations, a total number of $400 \times 128 \times 128$ grids, corresponding to a domain with scales of $8 \times 2.56 \times 2.56\ \mathrm{mm}^3$ (Fig. 1a), are used. The domain is a little wider than 0.01 times of the experimental setup of Sommerfeld and Qiu (1993). The finite volume method and the fractional-step projection technique (Chorin, 1968) are also applied. The spatial discretization scheme is of second-order precision. An explicit low-storage, third-order Runge–Kutta scheme (Williamson, 1980) is used for time integration. A direct fast elliptic solver is used to solve the Poisson equation. A typical result of λ_2-vortex (Jeong and Hussain, 1995) is showed on Fig. 1b, where the small discrete vortices are induced by the particle phase due to the feedback coupling effects.

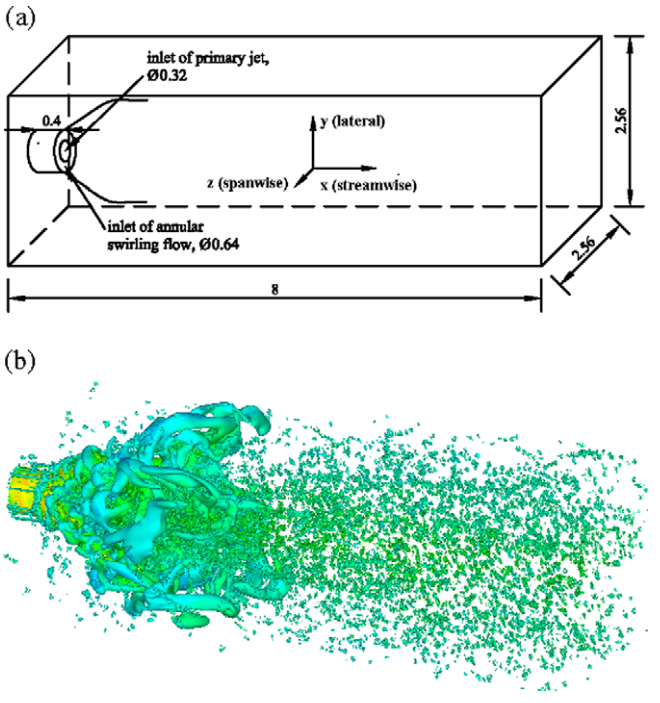

Fig. 1. (a) Sketch of numerical setup and its dimensions; (b) snapshot of λ_2-vortex for St = 22.38 at $t = 11$.

For DNS simulation, the requirement of grids increases exponentially with the Reynolds number ($Re^{3/4}$). According to Moin and Mahesh (1998), the largest scales is determined by the length of the simulation domain, and smallest scales that needs to be resolved is the commonly quoted Kolmogorov length scale η. However, this requirement is considered too stringent. In this study, as the mesh spacing is 0.02 mm, the resolved finest scales of turbulence by the central difference scheme are about 0.08 mm which is considered as within the range of $O(\eta)$. Thus, the spatial resolution for DNS is satisfied. Moreover, to stabilize the simulation for a strongly swirling flow, a fine time step of $\Delta t = 0.001$ and a total of 20,000 time steps are used.

2.2. Particle motion

The forces experienced by a isolated rigid particle suspended in a viscous quiescent carrier phase was firstly proposed by Tchen (1947), and it was corrected and modified into the well known Basset–Boussinesq–Oseen (BBO) equation. Maxey and Riley (1983) derived strictly a governing equation of motion of an isolated rigid spherical particle in an unsteady and non-uniform flow, in order to resolve the errors in previous versions of motion equation of particle. However, the equation is still very complicated. In the present study, some assumptions are considered: (1) Particles are treated as rigid spherical particles with a uniform diameter d_p and a uniform density ρ_p; (2) particle density is far larger than fluid density ($\rho_p/\rho_f \gg 1$); (3) As it is a dilute gas–solid flow and the loading of the particle is very small, the particle–particle collision effect is omitted. Based on the above assumptions, the Stokes drag force is of the leading order ($\rho_p/\rho_f \gg 1$, see Elghobashi and Truesdell, 1992). The Buoyancy force, Basset force, and virtual mass force are not of the leading order and omitted in simulation. The pressure gradient force and gravitational force are also not taken into account, since the fluid is incompressible and the gravity can be treated as absent in a vertical flow. However, the slip-shear lift force (Saffman, 1965; Mei, 1992) and the slip-rotation lift force (Crowe et al., 1998) are taken into account, since the rotation of particle and the gradient of fluid velocity play important roles in strongly swirling flows, both in the near-wall regions and in the central circulation zones.

As stated above, the particle phase is treated as a discrete dispersed phase, whose motion is simulated by integration of the Newton's law of motion,

$$\frac{d\mathbf{X}_p}{dt} = \mathbf{v}_p \tag{3}$$

$$m_p \frac{d\mathbf{v}_p}{dt} = \boldsymbol{f}_d + \boldsymbol{f}_{LR} + \boldsymbol{f}_{LS} \tag{4}$$

$$I_p \frac{d\boldsymbol{\omega}_p}{dt} = \mathbf{T} \tag{5}$$

where $\mathbf{X}_p$, $\mathbf{v}_p$ and $\boldsymbol{\omega}_p$ are coordinates, velocities and angular velocities of particles respectively. m_p and I_p are particle mass and moment of inertia, respectively. $\boldsymbol{f}_d$, $\boldsymbol{f}_{LR}$, $\boldsymbol{f}_{LS}$ and $\mathbf{T}$ are the drag force, the slip-rotation force, the slip-shear lift force, and the torques, respectively. They are expressed as following:

$$\boldsymbol{f}_d = \frac{1}{2}\rho_f \frac{\pi d_p^2}{4} C_D(\mathbf{u}-\mathbf{v}_p)|\mathbf{u}-\mathbf{v}_p| \tag{6}$$

$$\boldsymbol{f}_{LR} = \frac{\rho_f}{2}\frac{\pi}{4} d_p^2 C_{LR}|\mathbf{u}-\mathbf{v}_p| \frac{\boldsymbol{\Omega}\times(\mathbf{u}-\mathbf{v}_p)}{|\boldsymbol{\Omega}|} \tag{7}$$

$$\boldsymbol{f}_{LS} = 1.615 d_p^2 (\rho_f \mu_f)^{1/2} \left(\frac{1}{\omega_f}\right)^{0.5} \{(\mathbf{u}-\mathbf{v}_p)\times\boldsymbol{\omega}_f\} f(\mathrm{Re}_p, \mathrm{Re}_s) \tag{8}$$

$$\mathbf{T} = \frac{\rho_f}{2}\left(\frac{d_p}{2}\right)^5 C_R|\boldsymbol{\Omega}|\boldsymbol{\Omega} \tag{9}$$

where μ_f is fluid viscosity. C_D is the drag coefficient: $C_D = \frac{24}{\mathrm{Re}_p} f_d$, where Re_p is the particle Reynolds number $\mathrm{Re}_p = \frac{\rho_f d_p |\mathbf{u}-\mathbf{v}_p|}{\mu_f}$, and the factor f_d is set according to Clift et al. (1978): $f_d = 1 + 0.15\mathrm{Re}_p^{0.687} + 0.0175\frac{\mathrm{Re}_p}{1+4.25\times10^4 \mathrm{Re}_p^{-1.16}}$. The lift coefficient C_{LR} in Eq. (7) is a combination expression proposed by Rubinow and Keller (1961) and Oesterle and Dinh (1998):

$$C_{LR} = \begin{cases} \frac{d_p|\boldsymbol{\Omega}|}{|\mathbf{u}-\mathbf{v}_p|} = \frac{\mathrm{Re}_R}{\mathrm{Re}_p}, \text{for} \quad \mathrm{Re}_p \leqslant 1 \\ 0.45 + \left(\frac{\mathrm{Re}_R}{\mathrm{Re}_p} - 0.45\right)\exp\left(-0.05684\cdot \mathrm{Re}_R^{0.4}\cdot \mathrm{Re}_p^{0.3}\right), \\ \text{for} \quad 1 < \mathrm{Re}_p < 140 \end{cases} \tag{10}$$

where $\boldsymbol{\Omega} = \boldsymbol{\omega}_f - \boldsymbol{\omega}_p$ and $\omega_f = \frac{1}{2}\nabla\times\mathbf{u}$ are the difference of the rotational velocities between the fluid and the particle at locations where the particles occupy, and the rotational velocity of the fluid, respectively. Re_R in Eq. (10) is so-called the rotational Reynolds number of particle, and it is defined similarly as $\mathrm{Re}_R = \frac{\rho_f d_p^2 |\boldsymbol{\Omega}|}{\mu_f}$. The function $f(\mathrm{Re}_p, \mathrm{Re}_s)$ in Eq. (8) is explained as a ratio of the extended lift force to the Saffman lift force, and it is formulated as:

$$f(\mathrm{Re}_p, \mathrm{Re}_s) = \begin{cases} \left(1 - 0.3314\beta^{1/2}\right)\exp\left(-\frac{\mathrm{Re}_p}{10}\right) + 0.3314\beta^{1/2}, & \mathrm{Re}_p \leqslant 40 \\ 0.0524(\beta\mathrm{Re}_p)^{1/2}, & \mathrm{Re}_p > 40 \end{cases} \tag{11}$$

where Re_s is the shear Reynolds number, defined as $\mathrm{Re}_s = \frac{\rho_f d_p^2 |\omega_f|}{\mu_f}$, and β is a parameter, expressed as $\beta = \frac{d_p|\omega_f|}{2|\mathbf{u}-\mathbf{v}_p|} = \frac{1}{2}\frac{\mathrm{Re}_s}{\mathrm{Re}_p}$. At last, the coefficient C_R in Eq. (9) is given by Rubinow (1961), Sawatzki (1970) and Dennis et al. (1980):

$$C_R = \begin{cases} \frac{64\pi}{\mathrm{Re}_R}, & \text{for } \mathrm{Re}_R \leqslant 32 \\ \frac{12.9}{\mathrm{Re}_R^{0.5}} + \frac{128.4}{\mathrm{Re}_R}, & \text{for } 32 < \mathrm{Re}_R < 1000 \end{cases} \tag{12}$$

Before calculating all the above formulations, a non-dimensionalization process is carried out. Since, in the present study, the momentum coupling between the solid phase and the gas phase is done in dimensionless equations. After this process, the dimensionless motion equations for the particle phase are:

$$\frac{d\mathbf{v}_p}{dt} = \frac{f_D}{\mathrm{St}}(\mathbf{u}-\mathbf{v}_p) + \frac{3}{4}\frac{\rho_f}{\rho_p} C_{LS}\{(\mathbf{u}-\mathbf{v}_p)\times\boldsymbol{\omega}_f\} + \frac{3}{4}\frac{\rho_f}{\rho_p}\frac{\mathrm{Re}_p}{\mathrm{Re}_R} C_{LR}\{\boldsymbol{\Omega}\times(\mathbf{u}-\mathbf{v}_p)\} \tag{13}$$

$$\frac{d\boldsymbol{\omega}_p}{dt} = \frac{15}{16}\frac{\rho_f}{\rho_p \pi} C_R|\boldsymbol{\Omega}|\boldsymbol{\Omega} \tag{14}$$

where $\mathrm{St} = \frac{\rho d_p^2/(18\mu_f)}{L^*/U^*}$ is the Stokes number, defined as the ratio of particle response time to the characteristic time of fluid, and L^* and U^* are characteristic length scale and characteristic velocity. The characteristic length scale used here is according to Sommerfeld and Qiu (1993), and it is the distance from the primary jet inlet to the stagnation point at the top of the central recirculation bubble. The characteristic velocity is set according to the Reynolds number limitation. As a reduced value of Re = 669.4 is used, and based on the domain dimension and the fluid viscosity, the characteristic velocity is $U_1 = 15$ m/s here.

For integration of Eqs. (13) and (14) as time advances, an explicit step-forward scheme is used. At each time step after solution of the fluid field, the calculation of the right items of Eqs. (13) and (14) is done, and after that the updating of particle velocities and positions is carried out. During calculation of the right items of Eqs. (13) and (14), the feedback forces on each mesh cell are also calculated. Then, the feedback forces on each grid node (the vertices of the mesh cell) are obtained by a linear interpolation scheme.

2.3. Simulation conditions

As direct numerical simulation of high Reynolds number flow requires an exponentially huge number of numerical grids, it usually goes beyond the limitation of performance of computers. Thus, to carry out direct numerical simulation of a high Reynolds number flow following experimental conditions is out of the question. For example, the experiment carried out by Sommerfeld and Qiu (1993) is one of the most quoted experiments, with a Reynolds number of 52,400 which exceeds far from the limitation of computer performance. Hence, to follow the experimental conditions exactly for validation of numerical simulations is very difficult, although the similarity criterion is always used.

Thus, there are some different operating conditions between this numerical simulations and the experiment. For example, besides the difference in Reynolds number, we did not follow exactly the width and the geometry of the flow domain, since we used the Cartesian coordinates to simplify the tracking and simulating of particle motion.

However, we still tried to keep some key conditions similar to Sommerfeld and Qiu (1993) as a basic reference. For example, the ratio of diameters of the annular flow to that of the primary jet (D_2/D_1), the ratio of the axial velocities of the annular flow to that of the primary jet (U_2/U_1), the ratio of particle density to fluid density (ρ_p/ρ_f), the inflow velocity profiles, and the swirl number S, etc. The swirl number is the ratio of the axial flux of angular momentum to the axial flux of linear momentum:

$$S = \frac{2\int_0^{D_2/2} \rho w u r^2 dr}{D_2 \int_0^{D_2/2} \rho u^2 r dr}. \tag{15}$$

Unlike Sommerfeld and Qiu (1993), we used the diameter of the annular flow D_2 as the length scale in the denominator of Eq. (15), and obtained a large swirl number $S = 1.42$, which is corresponding to a strongly swirling flow.

To specify the inflow condition, the profiles of axial inflow velocity (Fig. 2a) is designed according to Sommerfeld and Qiu (1993) and the tangential velocity (Fig. 2b) is set according to Eq. (15). It is noticed that the tangential velocity within the range $|r| < R_2$ is also similar to the experiment. To use this type of inflow velocity configuration is reasonable since it captures the dominant characteristics of swirl velocity distribution. However, there are still other influencing factors, such as inflow turbulence intensity, which would significantly affect the vortex evolution. As the Reynolds number is relatively low, the initial turbulence is not evident or kept low. Moreover, we lack available experimental data which depicts the initial turbulence in detail. Thus, the present study did not introduce turbulence in the inflow condition, and the flows are evolved based on intrinsic characteristics of the swirl velocity distribution.

The other flow conditions and properties of fluid and particles, and the parameters for particles under different operating conditions are all listed in Tables 1 and 2. For different Stokes numbers, the particles are injected through the nozzle into the large container, and the number of particles for each injection depends on different Stokes numbers and particle sizes. The initial velocities of particles, including the angular velocity, are set the same as that of fluid where the particle occupies.

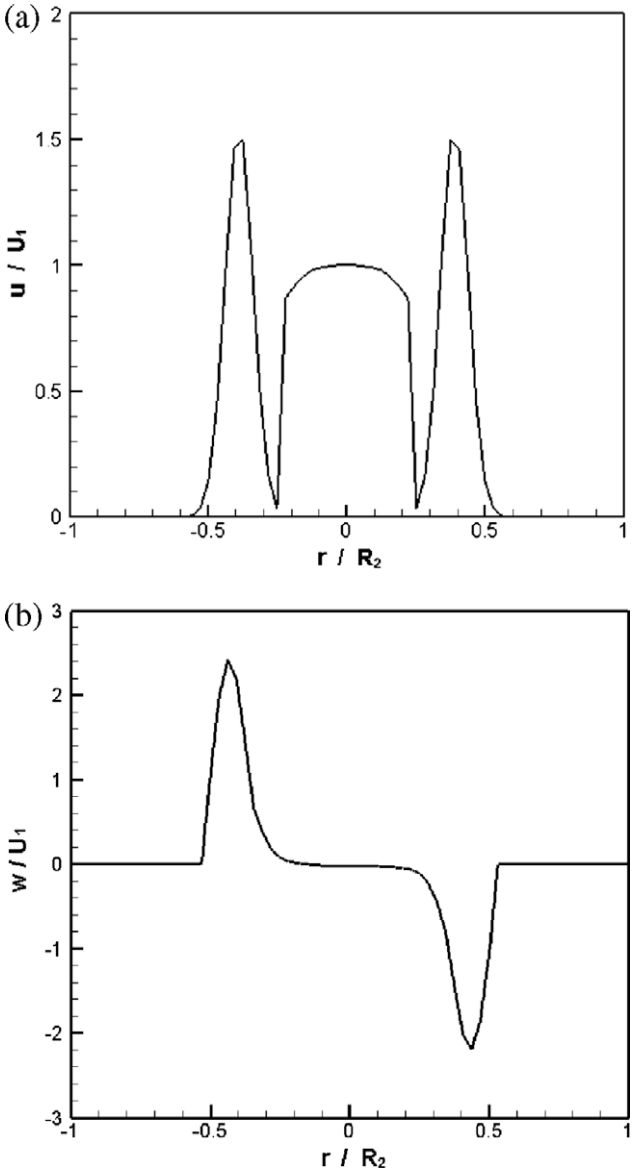

Fig. 2. Inflow axial (a) and tangential velocity profiles (b).

Table 1
Flow conditions and properties of fluid and particles.

Mean velocity of the primary flow	U_1 (m/s)	15
Mean velocity of the secondary annular flow	U_2 (m/s)	22.5
Diameter of the primary jet	D_1 (mm)	0.32
Diameter of the secondary annular flow	D_2 (mm)	0.64
Reynolds number	Re	669.4
Swirl number	S	1.42
Fluid viscosity	μ (Pa s)	$1.85 * 10^{-5}$
Ratio of densities for particle to fluid	ρ_p/ρ_f	2500/1.29

3. Numerical results

3.1. Partial validation

Firstly, as the experimental conditions are partially followed, a comparison of mean velocities of the gas phase at corresponding axial locations between this numerical simulation and the previous experiment (Sommerfeld and Qiu, 1993) is done to partially validate this simulation. However, the r.m.s. values of gas phase are not compared as it is greatly determined by the Reynolds number.

As Fig. 3a shows, as the inlet velocity profiles are similar and the swirl number is the same, the downstream development of velocity profiles is to some degree still alike, although the geometry of the flow domain and the Reynolds number are different. The peak values of mean velocity occur at the two sides, near the main stream of the annular flow, and a moderate flow flux occurs in

Table 2
Parameters for particles in different simulations.

Particle diameter D_p (μm)	Number of particles injected per time step	Stokes number S
1.73	777	0.46
2.57	236	1.02
7.42	10	6.79
8.98	6	10.38
12.02	2	22.28

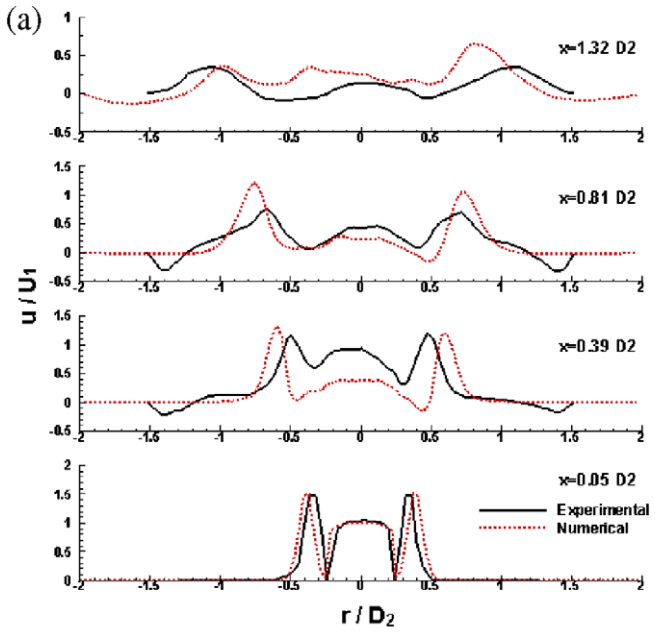

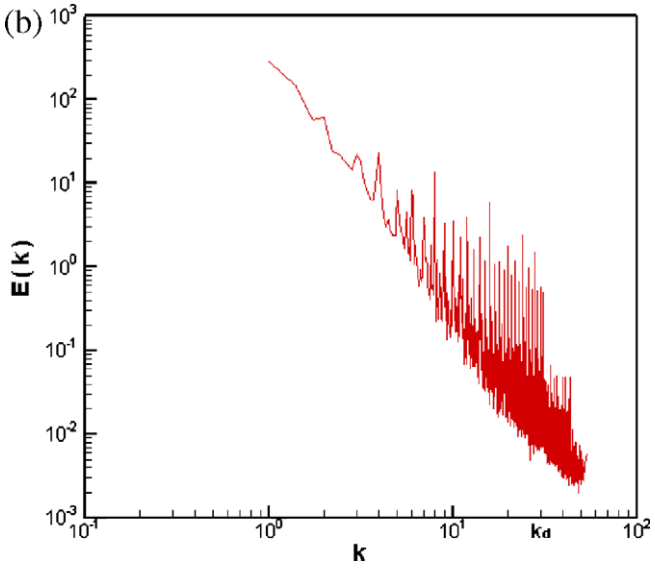

Fig. 3. (a) Comparison of mean gas velocity between this numerical study (Re = 669.41) and the referential experiment (Re = 52,400, Sommerfeld and Qiu) at four axial locations: $x = 0D_2$, $0.39D_2$, $0.81D_2$ and $1.32D_2$, respectively. The gas velocity is divided by the mean primary gas velocity U_1 and the radial coordinates is divided by the diameter of the annular swirling flow D_2. The width of numerical simulation is $4D_2$ whereas in experiment it is $3D_2$. It acts as only a partial validation; (b) the energy spectrum of fluid.

the central region of the primary jet. As the swirling flow for this study has a wider space and a slightly wider profile near the inlet ($x = 0.05D_2$), the downstream developments of the flow are also wider than that of experiment. Note that the inlet velocity profile is set according to the velocity profile of the experiment at $x = 0.05D_2$ ($z = 3$ mm in Sommerfeld and Qiu (1993)), therefore after evolution through the nozzle, the profile becomes wider than the experiments at $x = 0.05D_2$. Moreover, since the experimental swirling flow is of high Reynolds number and it is strongly restricted by the width of the container, minus velocities occur near the vicinity of the wall, whereas it did not occur so early in this simulation, until it reaches a further downstream location of $x = 1.32D_2$.

The similarities in development of velocity profiles are due to the fundamental characteristics of swirling flows in velocity profiles. Note that the type of bubble vortex breakdown is independent of the Reynolds number when the Reynolds number is small, and it occurs if and only if the swirl number reaches a critical value (Billant, 1998). Thus, in this way, the basic profiles of the swirling flow are to some degree similar with each other.

Secondly, to guarantee the quality of solution, Fig. 3c describes the energy spectrum of fluid which is obtained by fast Fourier transformation of the correlation functions:

$$E_{ij}(\mathbf{k}) = \int\int\int R_{ij}(\mathbf{r}) e^{-i\mathbf{k}\cdot\mathbf{r}} d^3\mathbf{r}$$

where $\mathbf{k}$ is the wave vector and $\mathbf{r}$ is the position vector. $R_{ij}(\mathbf{r}) = \overline{u_i(\mathbf{x})u_j(\mathbf{x}+\mathbf{r})}$ is the two-point correlation function and the over bar represents the ensemble average. As Fig. 3b shows, the Kolmogorov dissipation wave-number k_d is about 30 and the dissipation scale is $\eta = 1/k_d \approx 0.033$. The energy containing wave number k_{in} is less than 1 and consequently the energy containing scale l is larger than 1. Moreover, as the scale of the flow domain is $L = 4$ which indicates $l < L = 4$. As a result, the number of mesh grids in each dimension is required to be larger than $l/\eta = 121$. From this point of view, it is found that the spatial solution of fluid turbulence is fine enough.

3.2. Comparison of forces

In this section, we will demonstrate the relative importance of fluid-to-particle particles with different Stokes numbers. As Fig. 4 shows, we tracked and recorded the variation of different forces, i.e. the drag force, the slip-shear lift force and the slip-rotation lift force, respectively from $t = 0$ to 4, and then calculated mean values of the forces at each time point. From Fig. 4a, it is observed that the slip-shear lift force is of relatively secondary importance comparing to the drag force, i.e. it only reaches a maximum of 6% of the drag force. The relative importance of the slip-shear force increases with the Stokes number, which means the heavier the particle, the more important the slip-shear force. However, this trend seems to be attenuated by sufficient large particles, since from St = 6.79 to St = 22.28 the trend is not very evident.

The relative importance of the slip-shear force to the slip-rotation force is showed on Fig. 4b, from which we found that the relative importance depends largely on the Stokes number. For small particles, the slip-rotation force is less important than the slip-shear force, whereas for large particles the inverse becomes true. It seems to be true that for large particles the slip-rotation force is more important than the slip-shear force. It can even reach a superior limit comparative to the drag force provided the particle is large enough. Meanwhile, for small particles the slip-shear force becomes more important than the slip-rotation force, although under this condition both of them are relatively less important than the drag force, and could be neglected in simulation. This conclusion validates the simulation carried out by Sommerfeld and Qiu (1993), where only the drag force and the lift force due to particle rotation are considered under the condition of large Stokes numbers.

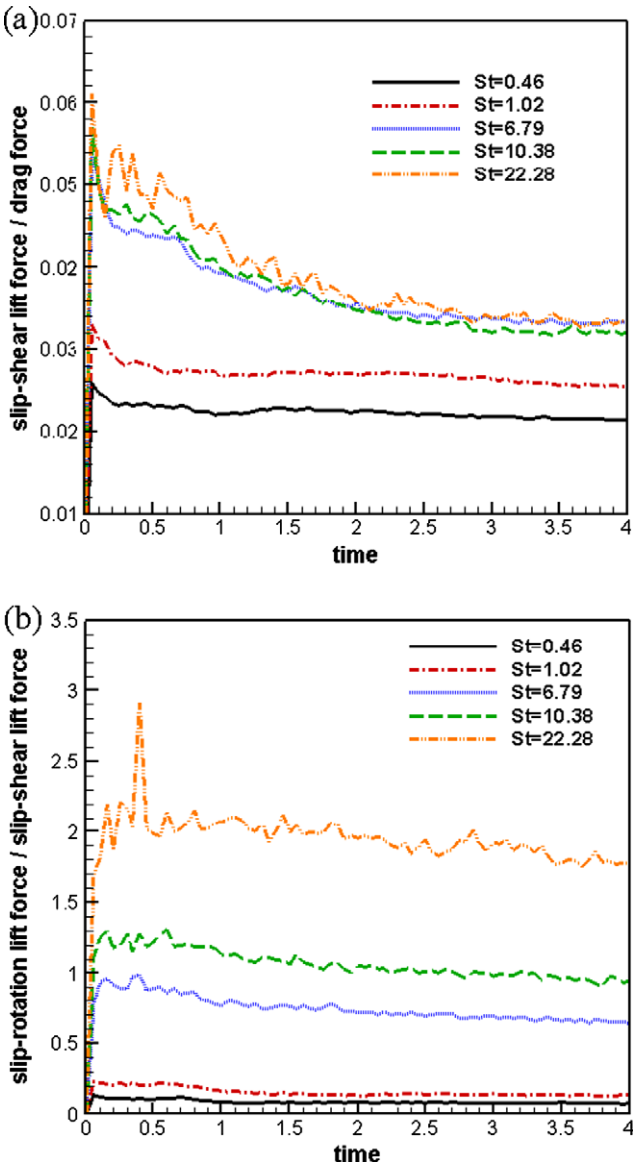

Fig. 4. Comparison of mean forces experienced by particle for $t = 0$–4. (a) Slip-shear lift force to drag force; (b) slip-rotation lift force to slip-shear lift force.

3.3. Particle velocity profile and fluctuation

To carry out statistics of particle phase, here we calculated statistically the time-averaged flow field of particles, based on the assumption of continuum of particle phase. The calculation is realized under the basis of locally-averaging treatment, which averages the physical quantities of particles within each discretized mesh cell, and regards it as a mass point of a continuum. To say more specifically, particle velocity $u_p(x,t)|_E$ at location x and time t on the basis of the Eulerian viewpoint (denoted as the subscript 'E') is calculated by a sum of velocity vectors of all the particles at time t within the mesh cell enclosing x. Then the mean and r.m.s values of particles are calculated just the same as fluid. Under this type of Eulerian point of view, the statistics of particle phase is then calculated easily. However, it is necessary to notice that the averaged profiles are not necessary to be smooth. It is reasonable since the averaging process is based on the Eulerian viewpoint. As the particles are in fact a discrete phase and the number of particles is relatively small, the profiles are certainly not as smooth as that of fluid.

Fig. 5a and b show the characteristics of the particle mean velocity profiles and fluctuations for different Stokes numbers at a typical axial location of about $x = 0.8D_2$ from the exit of the nozzle. The fluctuation is evaluated by the r.m.s. value of it. For large particles, the distribution of particles is almost concentrated near the central primary jet, although, in fact, there are many particles being dispersed by the expansion of vortex structure to the periphery of the primary jet. It is due to that heavy particles response to fluid more slowly and hardly than light particles before being transported downstream by the advection of the central primary jet. Comparatively, light particles with smaller Stokes number response to vortex structure sooner and they have enough time to follow the expansion motion of fluid vortex. Thus, they have a wider velocity profile and a wider distribution of intensive fluctuation than that of heavy particles.

Moreover, the absolute peak values of the mean velocity decrease as Stokes number increases, which means that with heavy particles suspended, the particle axial velocity become slower more rapidly than that suspended with light particles. It is reasonable since heavy particles have larger inertia and response to fluid more difficult and more slowly than light particles. This results in two straightforward effects: (1) The existence of heavy particles will act as blockages to the advection motion of the jet. (2) The slow-down of the jet will conversely lead to slow-down of the particles. For validation, Fig. 5c shows particle velocity on the central line of the primary jet. It is found that for large particles there exists a choke of the main stream. The particle velocities are not slowed down as smoothly as that of light particles. Alternatively, the particles move in a pattern of a quick slow-down, followed immediately with a quick speed-up, and then a smooth slow-down trend takes place. Moreover, the final slow-down takes place more quickly and then more slowly than the regular slow-down process of light particles. This kind of behavior will certainly cause an accumulation of particle near the region transited from the quick slow-down process to the quick speed-up process. It is so as showed on the inset of Fig. 5, which displays the particle number density on the central line. It is obvious that for large particles there exists a sudden raise in particle concentration near the predicted region.

The behavior of choke is due to the large inertia of particles which leads particle response to fluid vortex transition, i.e. the vortex expansion and recirculation of flow within the region of vortex breakdown, fairly sluggish. Thus, the bluntness of particle response can cause flow choke in the jet mainstream. On the other hand, the choke of flow in combustion industry may be beneficial to ignition of fuel, especially for coal particles, since the accumulation of fuel within the recirculation zone with a high temperature is an advantageous condition to fuel ignition and flame stabilization. From this point of view, for fuel mixtures with large inertia components are beneficial to stabilization of flame.

3.4. Particle Reynolds shear stress

The particle Reynolds stress is defined similarly as fluid, e.g. $\overline{u_i'u_j'}$, etc. $\overline{u'u'}, \overline{v'v'}, \overline{w'w'}$ are normal stresses and $\overline{u'v'}, \overline{u'w'}, \overline{v'w'}$ are shear stresses, where u', v' and w' are axial (streamwise), radial (lateral) and azimuthal (spanwise) component of turbulence fluctuation. In this section, we will demonstrate the three components of particle Reynolds shear stress, as the effect of the anisotropic nature of swirling flow on the shearing characteristics of particle behavior in Eulerian–Lagrangian direct numerical simulation has not been reported yet.

Fig. 6 shows the three components of particle shear stress in lateral direction at the same axial location of $x = 0.8D_2$ with dimensionless values. From Fig. 6a, it is showed that for particles with small Stokes numbers, the lateral (radial) dispersion is intensive than that with large Stokes numbers, especially in the region out

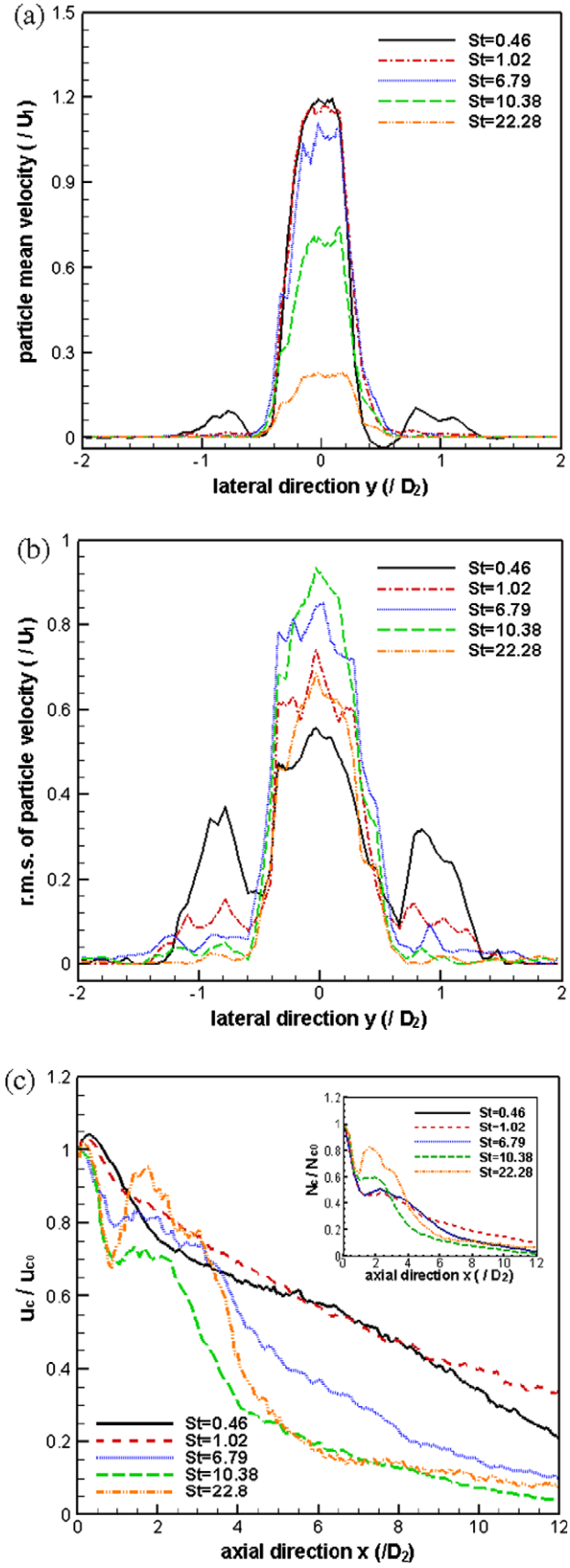

Fig. 5. Particle velocity profiles at different Stokes numbers: (a) particle mean velocity; (b) r.m.s. values of particle velocity and (c) particle velocity on the central line. The inset is the number density of particle on the central line. They are all non-dimensionlized by the values at the outlet of the nozzle.

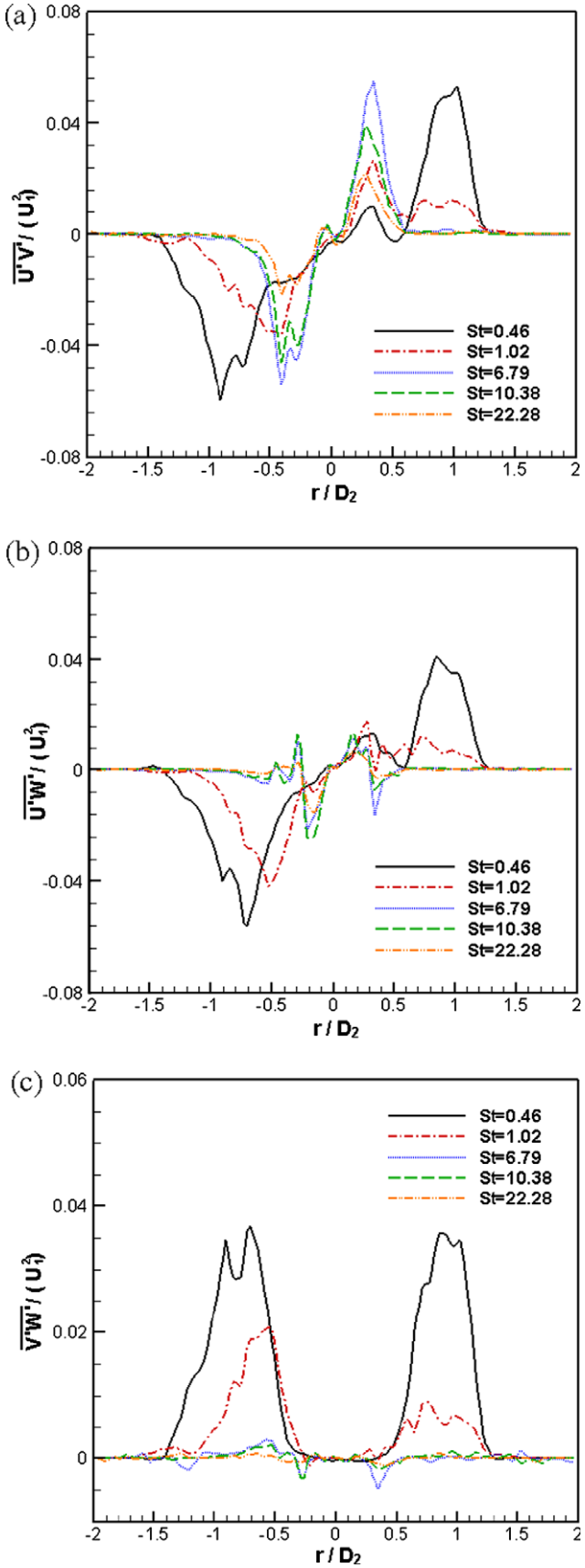

Fig. 6. Particle Reynolds shear stress in the lateral direction ($z = 0$) at an axial location of $x = 0.8D_2$. They are all non-dimensionalized by the square of the mean velocity of the primary jet: (a) $\overline{u'v'}/U_1^2$; (b) $\overline{u'w'}/U_1^2$; (c) $\overline{v'w'}/U_1^2$.

of the central main stream. Thus, though the axial component u' is very large for small particles within the range from $-0.5D_2$ to $0.5D_2$, the combination of $\overline{u'v'}$ within the same range is comparatively lower than that within $\pm(0.5 \sim 1.5)D_2$. In contrast, for large particles, the radial dispersion is less intensive due to their great inertia and slow response. As a result, the peak values of $\overline{u'v'}$ appear within the central mean stream ($-0.5D_2 \sim 0.5D_2$). For intermediate Stokes numbers ($St \approx 1$), both the above characteristics occur.

For $\overline{u'w'}$, similar results are observed in Fig. 6b for light particles. However, for heavy particles, it is showed by Fig. 6b that the azimuthal fluctuation seems to be much less intensive than the radial fluctuation. It indicates that for heavy particles it response to turbulence in the radial direction easily than that in the azimuthal direction. In other words, the motion behavior for heavy particles is characterized by a 'throw-away' pattern from the centre stream to the periphery following a helical trajectory with a weaker helicity, whereas the light particles can easily follow a strongly helical trajectory moving from the central main stream to its periphery. This difference in motion pattern characteristics can be easily explained by the difference in particle inertia. Since with the same moving velocities, particles with larger inertia have larger centrifugal tendencies, and need larger inter-phase forces to drive the particles to move in their previous directions. Under the same flow conditions, fluid cannot offer the required momentum to drive heavy particles in the same way as light particles.

For $\overline{v'w'}$, Fig. 6c shows the combination of $\overline{v'w'}$ and indicates that only for particles with light ($St < 1$) and intermediate Stokes numbers ($St \approx 1$) the radial and azimuthal velocities fluctuate in synchronism and with equivalent intensities. Otherwise, $\overline{v'w'}$ is almost negligible due to their fluctuation in different regions or inharmony of fluctuation intensity.

3.5. Particle turbulence intensity

As above-mentioned, the particle turbulence intensity is similarly defined as the r.m.s. values of particle velocity, namely $\sqrt{\overline{u'^2} + \overline{v'^2} + \overline{w'^2}}$ divided by the mean values of particle velocity $\sqrt{\bar{u}^2 + \bar{v}^2 + \bar{w}^2}$. In this way, the relative intensity of particle fluctuation from the Eulerian point of view is illustrated. For example, Fig. 7 shows three typical images of particle turbulence intensity at the same axial location of $x = 0.8D_2$.

Fig. 7a shows that particle fluctuation for small Stokes numbers ($St = 0.46$) is almost of smooth variation, just looks like a fluid motion. For each particle with large Stokes numbers, it is heavier than that with small Stokes numbers ($St \sim \rho_p d_p^2$ and $m_p \sim \rho_p d_p^3$). As a result, under the condition of same mass loading, the number of particles with small Stokes number is very larger than that of large Stokes number. Thus, the Eulerian statistical results of particle for small Stokes number are obviously smoother than that of larger Stokes number. Moreover, the variation of particle fluctuation for small Stokes number is inherently different from that of large Stokes number (Fig. 7c). It is observed from Fig. 7a that a coherent structure of particle distribution resembling a fluid vortex structure is established. It is a funnel-shaped rotating pattern in clock-wise direction, and it disperses particles from the centre to the periphery in a manner of helical motion. Fig. 7b shows a similar result for intermediate Stokes numbers. The pattern of distribution is similar to Fig. 7a, but with a small discrepancy that the particle turbulence intensity in the peripheral region is enhanced than Fig. 7a.

In contrast, for particles with great Stokes number, the distribution pattern seems to be greatly changed from the strongly helical structure to a more weak helical or even radial structure. As Fig. 7c

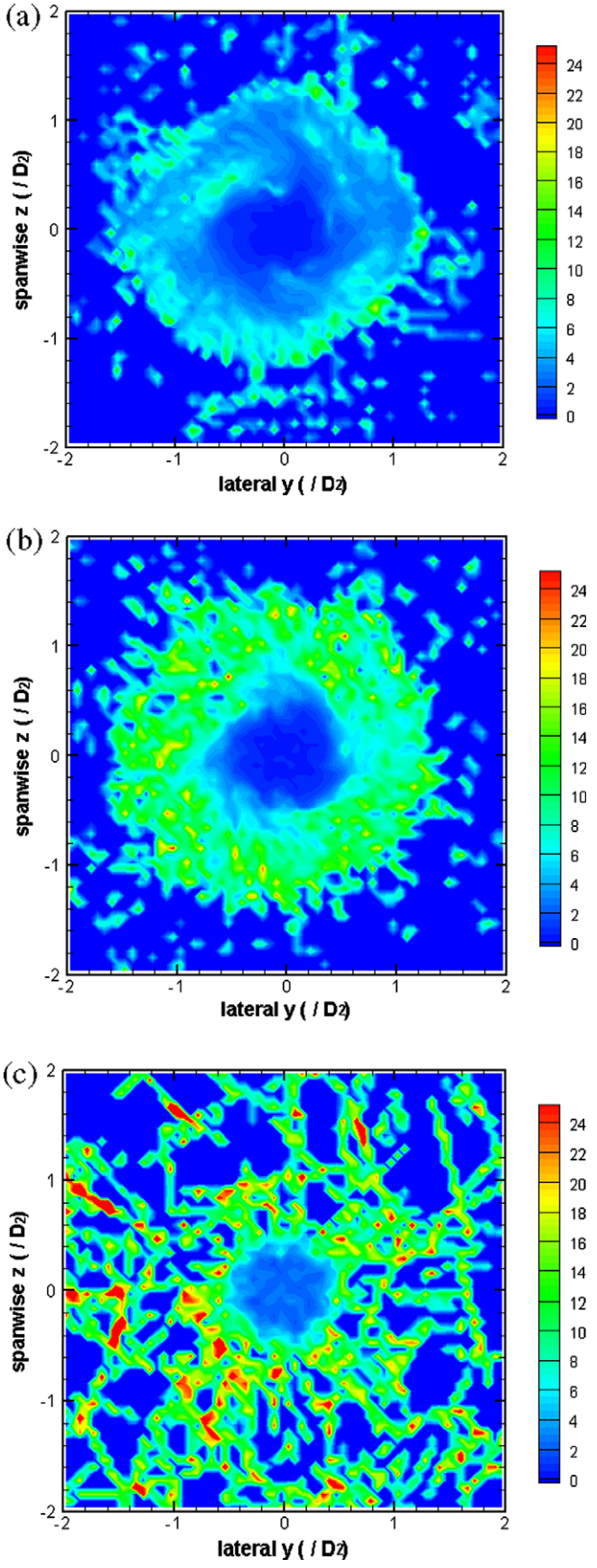

Fig. 7. Particle turbulence intensity in the axial location of $x = 0.8D_2$ at different Stokes numbers: (a) $St = 0.46$; (b) $St = 1.02$ and (c) $St = 27$.

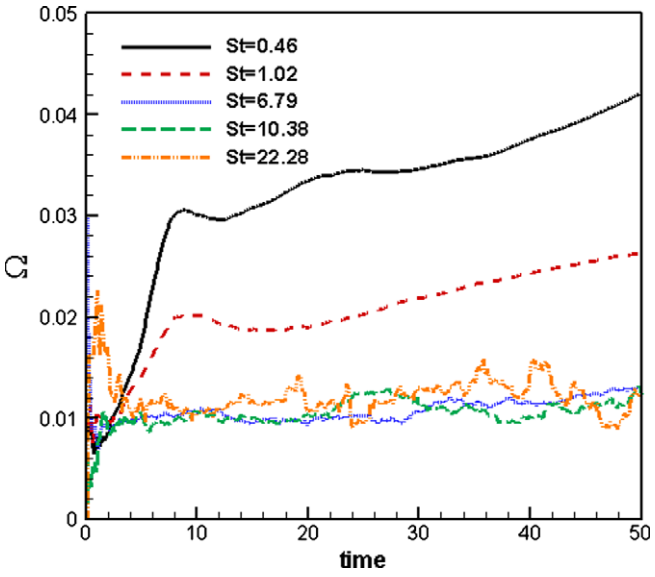

Fig. 8. The evolution of mean moment of particle momentum with respect to jet axis.

shows, the helical pattern of particle dispersion seems not to be as evident as before. Particle dispersion is greatly disturbed and particles can easily penetrate the periphery region of the swirling flow to the outer of the recirculation zones. A more homogeneous distribution in the peripheral region occurs, or alternatively a radial distribution is preferred. To describe it quantitatively, Fig. 8 shows the evolution of mean moment of particle momentum to the jet axis. The moment of particle momentum is defined as: $\Omega = \frac{1}{N_p}\sum_{n=1}^{N_p} \mathbf{r} \times \mathbf{v}_p$, where N_p is the number of particles. The moment of particle momentum quantifies the degree of rotational motion or helical motion of all the particles. It is observed from Fig. 8 that the rotational motion for particles with St = 0.46 and St = 1.02 are almost threefold and twofold intensive than that of the larger particles, respectively. That is why the great differences between pattern distributions of small and larger particles occur. This also validates the analysis of Fig. 6b in the above section, as it is mainly due to the great inertia of large particle for which fluid turbulence cannot drive it to move in a strong helical trajectory as easily as light particle.

The above results are based on the particle statistics in which the discrete phase of particles are localized and then averaged in the Eulerian approach. This technique is useful for revealing the behavior characteristics of dispersed phase in gas–solid flows.

4. Conclusion

The particle behaviors of different Stokes numbers in a strongly gas–solid swirling flow are studied by direction numerical simulation. The simulation makes reference to a previous experiment with some different conditions for the sake of easy numerical implementation. In this simulation, three fluid-to-particle forces (the drag force, the Magnus force, and the Saffman force) are considered and directly calculated. It is found after partial validation that:

(1) Although both the slip-shear lift force and slip-rotation lift force are of relatively secondary importance comparing to the drag force, the relative importance of them varies under diffident conditions. The importance of slip-shear force increases as the Stokes numbers. For small particles, the slip-rotation force is less important than the slip-shear force; for large particles the slip-rotation force is more important than the slip-shear force.

(2) The velocity profiles and fluctuations of particles at a typical axial location are demonstrated. Their differences indicate the different response characteristics of particles with different Stokes numbers. An interesting "choke" phenomenon in the mainstream for large particles are found and explained.

(3) Due to the anisotropic nature of the strongly swirling flow, the shear stress tensor cannot be neglected, even for particle motion. The anisotropic fluctuation of turbulence influences the particle shear Reynolds stress in different ways. The differences in the profiles of shear stress indicate the different pattern of particle dispersion in the swirling flow. It is concluded that both the particle motion and fluctuations and the shear stress characteristics are greatly correlated to the fluid turbulence.

(4) The particle turbulence intensity visualize the different patterns of particle dispersion. A strong helical motion for small particles and a weaker helical or even radial motion of larger particles are demonstrated respectively. For explanation, the mean moment of momentum of particles with respect to the jet axis quantifies the degree of helical motion of them.

Acknowledgement

This work was supported by the National Natural Science Foundation of China (Grant No. 50976101).

References

Apte, S.V., Mahesh, K., Moin, P., Oefelein, J.C., 2003. Large-eddy simulation of swirling particle-laden flows in a coaxial-jet combustor. Int. J. Multiphase Flow 29, 1311–1331.
Benjamin, T.B., 1962. Theory of the vortex breakdown phenomenon. J. Fluid Mech. 14, 593–629.
Billant, P., Chomaz, J.M., Huerre, P., 1998. Experimental study of vortex breakdown in swirling jets. J. Fluid Mech. 376, 183–219.
Candelier, F., Angilella, J.R., 2006. Analytical investigation of the combined effect of fluid inertia and unsteadiness on low-Re particle centrifugation. Phys. Rev. E 73, 047301.
Chorin, A., 1968. Numerical solution of the Navier–Stokes equations. Math. Comput. 22, 745.
Clift, R., Grace, J.R., Weber, M.E., 1978. Bubbles, Drops, and Particles. Academic Press, New York.
Crowe, C.T., Sommerfeld, M., Tsuji, Y., 1998. Fundamentals of Gas-Particle and Gas-Droplet Flows. CRC press.
Dennis, S.C.R., Singh, S.N., Ingham, D.B., 1980. The steady flow due to a rotating sphere at low and moderate Reynolds numbers. J. Fluid Mech. 101, 257–279.
Elghobashi, S., Truesdell, G.C., 1992. Direct simulation of particle dispersion in a decaying isotropic turbulence. J. Fluid Mech. 242, 655–700.
Escudier, M.P., Zehnder, N., 1982. Vortex flow regimes. J. Fluid Mech. 115, 105–121.
Grauer, R., Sideris, T.C., 1991. Numerical computation of 3D incompressible ideal fluids with swirl. Phys. Rev. Lett. 67, 3511–3514.
Herrada, M.A., Shtern, V., 2003. Vortex breakdown control by adding near-axis swirl and temperature gradients. Phys. Rev. E 68, 041202.
Jeong, J., Hussain, F., 1995. On the identification of a vortex. J. Fluid. Mech. 285, 69–94.
Liang, H., Maxworthy, T., 2005. An experimental investigation of swirling jets. J. Fluid Mech. 525, 115–159.
Maxey, M.R., Riley, J.J., 1983. Equation of motion for a small rigid sphere in a nonuniform flow. Phys. Fluids 26 (4), 883–889.
Mei, R., 1992. An approximate expression for the shear lift force on spherical particles at finite particle Reynolds number. Int. J. Multiphase Flow 18 (1), 145–147.
Moin, P., Mahesh, K., 1998. Direct numerical simulation: a tool in turbulence research. Annu. Rev. Fluid Mech. 30, 539–578.
Oefelein, J.C., Sankaran, V., Drozda, T.G., 2007. Large eddy simulation of swirling particle-laden flow in a model axisymmetric combustor. Proc. Combust. Inst. 31, 2291–2299.
Oesterle, B., Dinh, T.B., 1998. Experiments on the lift of a spinning sphere in a range of intermediate Reynolds numbers. Exp. Fluids 25, 16–22.
Park, T.W., Katta, V.R., Aggarwal, S.K., 1998. On the dynamics of a two-phase nonevaporating swirling jet. Int. J. Multiphase Flow 24, 295–317.
Rubinow, S.I., Keller, J.B., 1961. The transverse force on a spinning sphere moving in a viscous fluid. J. Fluid Mech. 11, 447–459.
Saffman, P.G., 1965. The lift on a small sphere in a slow shear flow. J. Fluid Mech. 22, 385–400.
Sawatzki, O., 1970. Strömungsfeld um eine rotierend Kugel. Acta Mech. 9, 159–214.
Shirolkar, J.S., McQuay, M.Q., 2001. A PDF propagation approach to model turbulent dispersion in swirling flows. Eur. J. Mech. B – Fluids 20, 699–726.

Shtern, V., Goldshtik, M., Hussain, F., 1994. Generation of swirl due to symmetry breaking. Phys. Rev. E 49, 2881–2886.
Shtern, V., Mi, J., 2004. Hysteresis and precession of a swirling jet normal to a wall. Phys. Rev. E 69, 016312.
Sommerfeld, M., Qiu, H.H., 1993. Characterization of particle-laden, confined swirling flows by phase-doppler anemomentry and numerical calculation. Int. J. Multiphase Flow 19, 1093–1127.
Subramanian, G., Koch, D.L., 2006. Centrifugal forces alter streamline topology and greatly enhance the rate of heat and mass transfer from neutrally buoyant particles to a shear flow. Phys. Rev. Lett. 96, 134503.
Tchen, C.M., Ph.D. thesis, Delft, Martinus Nijhoff, The Hague, 1947.
Wicker, R.B., Eaton, J.K., 2001. Structure of a swirling, recirculating coaxial free jet and its effect on particle motion. Int. J. Multiphase Flow 27, 949–970.
Williamson, J., 1980. Low-storage Runge–Kutta schemes. J. Comput. Phys. 35, 48.